

3D-MHD simulations of an accretion disk with star-disk boundary layer

Adriane Steinacker

NASA Ames Research Center, Moffett Field, CA 94035

`adriane@duras.arc.nasa.gov`

John C.B. Papaloizou

*Astronomy Unit, School of Mathematical Sciences, Queen Mary and Westfield College,
Mile End Road, London E1 4NS*

`J.C.B.Papaloizou@maths.qmw.ac.uk`

ABSTRACT

We present global 3D MHD simulations of geometrically thin but unstratified accretion disks in which a near Keplerian disk rotates between two bounding regions with initial rotation profiles that are stable to the MRI. The inner region models the boundary layer between the disk and an assumed more slowly rotating central, non magnetic star. We investigate the dynamical evolution of this system in response to initial vertical and toroidal fields imposed in a variety of domains contained within the near Keplerian disk. Cases with both non zero and zero net magnetic flux are considered and sustained dynamo activity found in runs for up to fifty orbital periods at the outer boundary of the near Keplerian disk.

We find a progression of behavior regarding the turbulence resulting from the MRI and the evolving structure of the disk and boundary layer according to the initial field configuration. Simulations starting from fields with small radial scale and with zero net flux lead to the lowest levels of turbulence and smoothest variation of disk mean state variables. As found in local simulations, the final outcome is shown to be independent of the form of the imposed field. For our computational set up, average values of the Shakura & Sunyaev (1973) α parameter in the Keplerian disk are typically 0.004 ± 0.002 . Magnetic field eventually always diffuses into the boundary layer resulting in the build up of toroidal field, inward angular momentum transport and the accretion of disk material. The mean radial velocity, while exhibiting large temporal fluctuations is always subsonic.

Simulations starting with net toroidal flux may yield an average $\alpha \sim 0.04$. While being characterized by one order of magnitude larger average α , simulations starting from vertical fields with large radial scale and net flux may lead to the formation of persistent non-homogeneous, non-axisymmetric magnetically dominated regions of very low density. In these gaps, angular momentum transport occurs through magnetic torques acting between regions on either side of the gap. Local turbulent transport occurs where the magnetic field is not dominant. These simulations are indicative of the behavior of the disk when threaded by magnetic flux originating from an external source. However, the influence of such presumed sources in determining the boundary conditions that should be applied to the disk remains to be investigated.

Subject headings: accretion, accretion disks — MHD, instabilities

1. Introduction

The study of the boundary layer, the region where the angular velocity of an accretion disk drops to match the rotation velocity of the central object, is of great importance for the understanding of accreting objects, since up to half of the total accretion energy can be released there (Lynden-Bell & Pringle 1974) if the central object is a slow rotator. Up to now detailed studies of this region (eg. Papaloizou & Stanley 1986, hereafter PS, Kley 1989, Popham & Narayan 1992) have been based on the Navier-Stokes equations with a modified viscosity prescription involving an anomalous viscosity coefficient. This is presumed to contain the effects of any turbulence present reducing the problem to one of laminar flow.

The decrease of angular velocity in the boundary layer is associated with an increase in the thermal pressure, which replaces centrifugal support for the accreting matter. The large pressure gradients in turn, may be associated with supersonic radial infall velocities in this region, if a standard disk viscosity prescription is continued into the layer. However, it has been argued that if such a supersonic flow occurred, the star would loose its causal connection to the outer disk (Pringle 1977). In relation to this issue, several studies based on the Navier-Stokes equations were performed but with a modified viscosity prescription in the boundary layer corresponding to its much lower pressure scale height (PS, Popham & Narayan 1992). This modification alone does not eliminate supersonic flows under all conditions (e.g. for large values of $\alpha \simeq 1$). Popham & Narayan (1992) suggested reducing the viscosity coefficient to zero as the radial infall velocity approaches the sound speed. This causally limited viscosity (Narayan 1992) always leads to subsonic infall. A different approach, appreciating the short time required for matter to pass through the layer, allows the viscous stress components

to relax towards their equilibrium values on a relaxation time scale (Kley & Papaloizou 1997) and so naturally incorporates causality. Studies of one-dimensional models led to the conclusion that the boundary layer must be characterized not only by the value of α in the outer disk, but also by the nature of the viscous relaxation process. Additional time dependent studies demonstrated that for low $\alpha \simeq 0.01$, the boundary layer adjusts to a steady state, while for large $\alpha = 0.1$, significant disturbances occurred in the boundary layer and to the power output. Periodic oscillations were seen throughout the disk by PS, whenever α was large (close to 1). For small α , the oscillations were localized near the outer disk boundary. These oscillations are caused by the viscous overstability found by Kato (1978) and Blumenthal et al. (1984) and it was suggested they may be important in explaining the time-dependent behavior in accreting objects such as CVs and protostars.

All of the above models were based on an ad-hoc anomalous viscosity prescription and did not consider further its origin. The discovery of the relevance of the magnetorotational instability (MRI) (Balbus & Hawley 1991) has opened up a new era in accretion disk astrophysics. The instability provides a robust and self-consistent mechanism for the production of turbulence and angular momentum transport in these objects if they are adequately ionized, thereby removing the need for ad-hoc prescriptions. The development of different numerical codes has enabled a detailed investigation of the nonlinear phase of the instability. First numerical studies were performed in a local shearing box approximation, (Hawley, Gammie & Balbus 1995, Brandenburg et al. 1995, Sano, Inutsuka & Miyama 1998, Fleming, Stone & Hawley 2000, Miller & Stone 2000). These studies show that the turbulent outcome of the MRI depends on the initial field configuration applied to the disk. Thus, local simulations with initial vertical fields with zero net flux field indicate an average $\alpha = 0.001 - 0.006$, while vertical fields with non zero net flux result in larger values of α up to 0.3. The turbulent outcome of an initially unstable toroidal field can lead to intermediate values of α up to 0.04 depending on the net flux.

Relatively recently studies of instabilities in global disk models have begun (Armitage 1998). Such studies are needed to see how an unstable disk modifies its underlying structure in response to globally varying levels of turbulence and whether the longer time scale evolution is in any way like that of standard ' α ' disk models. Recent studies have been made by Hawley (2000), who concentrated on the evolution of thick tori, and Hawley & Krolik (2001). The latter study focuses on the evolution of the inner region of a disk accreting onto a black hole modeled with a pseudo-Newtonian potential.

In this paper we study the interaction of an accretion disk with a boundary layer region located between it and the central star. This situation is the relevant one to consider for non relativistic accretion onto a non magnetic central star. The inner boundary layer region

together with an exterior stable region also provide convenient, relatively inert regions in which to embed a near Keplerian disk with an unstable rotation profile. Instead of prescribing the viscosity in an ad-hoc fashion, as in previous studies of the boundary layer, we self-consistently incorporate the turbulence arising from the MRI as the source of viscosity and diffusion of magnetic field.

We assume the disk to have a small ratio of scale height to radius ($H/R \simeq 0.1$). The gravity is assumed to be entirely due to the central object and for simplicity and in common with other global disk studies we neglect vertical stratification by adopting a cylindrically symmetric potential thus focusing the study on the radial structure of the disk. We study the dynamical evolution of the disk over a time span of up to one thousand rotation periods measured at the inner disk edge. We consider different initial magnetic field configurations (poloidal and toroidal) imposed in the main body of the disk. Cases with both non zero and zero net magnetic flux are considered.

Simulations starting with small scale initial fields with zero net flux exhibit the lowest Shakura & Sunyaev (1973) parameter α with a mean value averaged over the Keplerian domain of $\simeq 0.005$. In this case the simulations on average attain a final state characterized by the same mean α and magnetic energy independently of (within computationally defined limits) the initial field strength. There may also be a tendency for the mean value of α to increase with the extent of the vertical domain and the numerical resolution. This is in agreement with results of shearing box simulations (Hawley, Gammie & Balbus 1996, hereafter HGB96). On the other hand simulations with large net magnetic flux may evolve turbulence with a larger mean value of α of $\simeq 0.04$, when the initial field is toroidal. Models starting from initial vertical fields with large radial scale are such that α attains maximum values > 1 in regions associated with prominent density depressions, while outside these gaps, α reaches values similar to the zero net flux models (as low as 0.005). The volume averaged α depends on the initial plasma beta in such cases.

We find that all simulations locally exhibit strong variations of the vertically and azimuthally averaged values of α in time and with radius. All of the models display oscillations of the vertically and azimuthally averaged radial Mach number. Even though the boundary layer region is stable to the MRI, magnetic field always diffuses into it. This is the case even when the initial field is non zero only well away from the layer. Toroidal field build up enables mass to accrete through it onto the central star through the operation of magnetic torques.

The paper is organized as follows: in §2 we present the basic model and computational set up. In §2.1 we describe the numerical procedure. In §3 we discuss azimuthal and vertical averaging together with the global transport of angular momentum and energy dissipation in the disk. §4 is devoted to the investigation of cases with initial fields with zero net magnetic

flux. In §5 we present results when the initial magnetic field has net flux. Finally, we summarize our results in §6.

2. Initial model setup

The simulations are performed within the framework of ideal MHD. The governing equations are:

$$\frac{\partial \rho}{\partial t} + \nabla \cdot \rho \mathbf{v} = 0, \quad (1)$$

$$\rho \left(\frac{\partial \mathbf{v}}{\partial t} + \mathbf{v} \cdot \nabla \mathbf{v} \right) = -\nabla p - \rho \nabla \Phi + \frac{1}{4\pi} (\nabla \times \mathbf{B}) \times \mathbf{B}, \quad (2)$$

$$\frac{\partial \mathbf{B}}{\partial t} = \nabla \times (\mathbf{v} \times \mathbf{B}). \quad (3)$$

where all the quantities have their usual meanings. While in some of our exploratory simulations we adopted an adiabatic equation of state (with heating due to artificial viscosity retained), the runs described in this paper are either based on using a locally isothermal equation of state, i.e.

$$P(R) = \rho(R) \cdot c(R)^2, \quad (4)$$

where $c(R)$ denotes the sound speed in the disk specified as a fixed function of R , or after using this initially, solving the energy equation assuming that heating due to artificial viscosity is removed by an exactly compensating cooling. Either of those procedures gave very similar results. We found them to lead to a more consistent procedure since the numerical scheme currently applied with zero resistivity does not allow for magnetic energy dissipated on the grid scale to be recovered as heat. Tests showed that when an adiabatic condition was used, such that kinetic energy dissipated through an artificial viscosity was recovered as heat, there was a noticeable change in the thermal energy content in the Keplerian disk during the course of a simulation.

The computations are carried out in cylindrical coordinates (z, R, ϕ) . We assume that the gravitational potential is only dependent on the radial coordinate, $\Phi = -GM/R$, where M is the mass of the central object and G is the gravitational constant.

Our computational domain is divided into three distinct regions: 1) An extended active Keplerian domain, ranging from a radius R_1 to R_2 , in which the growth of the MRI leads to turbulence (Region I); 2) An inner boundary layer ranging from R_0 , the lower radial boundary of the computational domain, to R_1 (Region II), and 3) an outer region ranging from R_2 to the outer radial boundary, which we have added to avoid numerical problems with trying to apply a boundary condition directly at the outer edge of the active domain

(Region III). The corresponding values of R_1 , R_2 and R_3 are specified in table 1. The initial density and angular velocity profiles for these three regions are calculated consistently with hydrostatic equilibrium in the radial direction. We present these solutions below.

Region I: $R_1 \leq R < R_2$. In contrast to previously published cylindrical global accretion disk simulations (Armitage 1998, Hawley 2000 and Hawley & Krolik 2001) where constant density profiles were used, we adopt a density varying inversely with the radial distance

$$\rho(R) = \rho_0 \cdot R_0/R, \quad (5)$$

and a radial dependence of the sound speed given by

$$c(R) = c_0 \sqrt{R_0/R} \quad (6)$$

where ρ_0 and c_0 are the density and sound speed corresponding to the radial position R_0 . With the pressure determined by a locally isothermal equation of state, we calculate the rotation velocity

$$v_\phi(R) = \sqrt{GM/R_0 - 2c_0^2} \cdot \sqrt{R_0/R}. \quad (7)$$

For a thin disk in which the sound speed at a given radius is much smaller than the rotation velocity, this profile is nearly Keplerian.

Region II: $R_0 \leq R \leq R_1$. In this region we require the angular velocity Ω to drop from its near-Keplerian value at $R = R_1$ to a lower value Ω_* which can be considered as matching the angular velocity of a central stellar object. For the rotation velocity, setting $i = 1$, we adopt

$$v_\phi(R) = v_{\phi i} \cdot (R/R_i)^{n_b}, \quad (8)$$

and for the sound speed we take

$$c(R) = c_i (R_i/R)^{n_c}. \quad (9)$$

These prescriptions lead to the following density profile:

$$\rho(R) = \rho_i \cdot (R/R_i)^{2n_c} \cdot \exp \left[\frac{0.5\delta - 1}{n_b + n_c} \cdot ((R/R_i)^{2(n_b+n_c)} - 1) - \delta \cdot f_i(R) \right], \quad (10)$$

where $f_i(R) = \ln(R/R_i)$, if $n_c = 0.5$, and $f_i(R) = [(R/R_i)^{2n_c-1} - 1] / (2n_c - 1)$, otherwise, and $\delta = GM/(R_0 c_0^2)$. Here ρ_i , c_i and $v_{\phi i}$ are the density, sound speed, and rotation velocity, at the radius R_i . These quantities are given by eq. (5), (6) and (7), respectively. We have considered cases with $n_b = 1$ (corresponding to uniform rotation), $n_b = 2$ and $n_b = 3$. When $n_b = 2$, we took $n_c = 0$. When $n_b = 1$, or $n_b = 3$ we took $n_c = 0.625$ in most of the cases. Situations with $n_c = 0.5$ have also been considered. We note that tests showed that when

this region was initiated with a density profile not too far out of hydrostatic equilibrium, the situation rapidly adjusted so that such an equilibrium was attained.

Region III: $R_2 < R \leq R_3$. This region is added primarily for numerical stability. It provides a high inertia which prevents the magnetic field from diffusing into the outer radial boundary and producing a severe drop in the density and angular velocity of the boundary zones during the course of the simulations. This would ultimately contaminate the global energetics, leading to incorrect behavior of the magnetic energy and the α parameter. In this region, the solutions presented above for region II continue to be valid, but with the index $i = 2$. In practice we adopted uniform initial rotation profiles that are stable with respect to the MRI ($n_b = 1$) and $n_c = 0.5$.

The assumption of a thin disk requires the sound speed to be smaller than the rotation velocity, which is equivalent to the pressure scale height $H = c/\Omega$, the disk would have if stratified vertically, being significantly less than the current radius. We chose $c_0^2 = 0.01GM/R_0$ for most models but also ran two (b4,b5) with $c_0^2 = 0.04GM/R_0$ for comparison purposes.

We comment that due to the chosen radial dependence of the sound speed and rotational velocity in region I, the scale height H is a linear function of R . In most cases we chose the extent of the computational domain in z to be larger than one scale height at the outer radial edge of the Keplerian domain. In few cases this was taken to be one half of the scale height at the outer radial boundary of the Keplerian domain, thus allowing us to test the effect of the extent of the z domain on the results.

For most calculations with zero net flux fields, the radial domain was chosen such that $R_1 = 1.2, R_2 = 3.7$ and $R_3 = 4.5$. The ϕ -domain extends from 0 to $\pi/2$ in most models. Recent work by Hawley (2001) suggests that, with the same resolution, the extent of the ϕ domain does not greatly affect the results. We have checked this by performing runs with the ϕ domain extending to π , and $\pi/3$. The boundary conditions in z and ϕ are periodic. In R we set the scalar quantities, magnetic field components and z - and ϕ -components of the velocity to have zero gradient. The radial velocity components at the inner and outer radial boundaries were set to zero. This ensures mass conservation in the computational domain. We also note that the computational set up is such that the zero gradient condition on the azimuthal velocity applied at the radial boundaries only affects values at ghost zones that do not affect the flow elsewhere. Thus artificially imposed viscous boundary layer effects do not occur in our calculations.

We have performed simulations with:

1. Initial vertical fields with and without net flux,

2. Initial toroidal fields with and without net flux,

the magnetic field being initially defined in a restricted radial domain:

$$\mathbf{B}_i = B_0 \sin \left(2n_R \pi \frac{R - R_b}{R_{b1} - R_b} \right) \mathbf{e}_i, \quad (11)$$

with $n_R = 0.5, 1.5$ for net field runs, and $n_R = 3, 6, 9$ for runs with zero net flux. The index i indicates either the vertical or the toroidal field component with the corresponding unit vector \mathbf{e}_i . For toroidal fields B_0 is a constant while for vertical fields $B_0 \propto 1/R$, with R_b and R_{b1} being the boundaries of the region where the field was applied. These will be specified for each run in turn.

An overview of the performed simulations is given in table 1, which shows the magnetic field topology used, the mean plasma beta defined as the ratio of thermal to magnetic pressure with each of these averaged over the Keplerian domain, the numbers of computational grid points in each direction, the number of wavelengths of the mode of maximum growth for the MRI contained in the z-domain (z_u and z_l being the upper and lower boundaries) at the location of the innermost field maximum, the number of wavelengths in radial direction, n_R , specified in order to define the net and zero net flux fields, respectively, the location of the boundaries to the three different regimes of the R-domain, R_1, R_2 and R_3 , the extent of the domain in ϕ and z , and the duration of the run in units of the inverse Keplerian angular frequency at the inner boundary located at $R_0 \equiv 1$. Typically the runs last for about 20 orbits measured at the outer radius of the active Keplerian region located at $R \sim 4$, although we performed one long run for a larger disk with $R_2/R_0 = 7.2$ for a time exceeding 50 orbits at the outer boundary of the Keplerian domain in order to confirm the persistence of the turbulence up to such times. For computational purposes, the unit of length is taken to be the inner boundary radius, thus $R_0 = 1$, the unit of mass is the central mass, and the unit of time is the inverse Keplerian angular frequency at the inner boundary radius, or the period there divided by 2π .

2.1. Numerical procedure

The numerical procedure follows the method of characteristics constrained transport MOCCT as outlined in Hawley & Stone(1995) and implemented in the ZEUS code. Alfvén wave characteristics are used to integrate the induction equation and to evaluate the Lorentz force. The evolution of the magnetic field, \mathbf{B} , is constrained to enforce $\nabla \cdot \mathbf{B} = 0$ to machine accuracy. The code has been developed from a version of NIRVANA originally written by U. Ziegler (see Ziegler & Rüdiger 2000 and references therein), and has been previously used for 2D

hydrodynamic simulations of viscous disks interacting with migrating Jovian mass planets. The results have been validated by detailed comparison with other codes and independently obtained results (Bryden et al. 1999, Nelson et al. 2000, Kley, Angelo & Henning 2001). Shearing box MHD simulations have also been performed by Ziegler & Rüdiger (2000).

The time step is limited by the Courant condition. In addition, we have implemented the numerical technique used by Miller & Stone (2000) to prevent the time step becoming too small by not allowing the Alfvén speed to exceed a limiting value in regions of very low density. Tests have shown that this makes no significant difference to the results obtained, while circumventing the severe drop in the time step which would sometimes make practical continuation of simulations impossible. We also set a global floor for the density. On performing a series of exploratory runs with different values for the limiting speed and the density floor, we found that simultaneous application of the two methods leads to the best results in a most economical manner. However, as stated above, the results were unaffected by reasonable changes to the floor or the limiting velocity. For the runs listed in table 1, the density floor was $\rho_{fl} = 10^{-3}\rho_0$ and the limiting velocity was $v_{lim} = 0.3$.

In all cases, the instability was initiated by applying a sinusoidal perturbation in the radial velocity with an amplitude of $0.01c_0$. The number of wavelengths in the vertical domain of the most unstable MRI mode calculated for the initial field at the location of the innermost field maximum varies between 1 and 6 as specified in column 5 of table 1. The wavelength associated with the mode of maximum growth was calculated from

$$\lambda_{max} = \sqrt{\frac{16\pi}{15}} \frac{B}{\sqrt{\rho}\Omega}. \quad (12)$$

We note that due to the radial dependences of the density, angular velocity and magnetic field, λ_{max} is a function of radius. If λ_{max} is smaller than the extent of the z domain, in the case of vertical fields, regions of stability may alternate with unstable regions.

3. Angular momentum transport

In order to describe the behavior of the different models, it is helpful to use quantities that are vertically and azimuthally averaged over the (ϕ, z) domain. These are defined with an overbar such that for any quantity Q

$$\overline{Q(R, t)} = \frac{\int \rho Q dz d\phi}{\int \rho dz d\phi}. \quad (13)$$

Note that although the numerical simulations are done over a fraction of the full ϕ domain, because of periodicity they can be stacked end to end so that without loss of generality we

run	B	$\langle\beta\rangle$	$N_z \times N_R \times N_\phi$	$\frac{z_u - z_l}{\lambda_{max}}$	n_R	R_1	R_2	R_3	ϕ	z	time
b1	0-net B_z	105	$36 \times 334 \times 108$	2	6	1.2	3.7	4.5	$\pi/2$	± 0.2	526
b2	—	316	$36 \times 334 \times 108$	4	—	—	—	—	—	—	592
b3	—	1005	$36 \times 334 \times 108$	6	—	—	—	—	—	—	697
b4	—	143	$36 \times 167 \times 108$	0.5	3	1.5	—	—	—	—	710
b5	0-net B_ϕ	32	$36 \times 167 \times 108$	0.3	—	—	—	—	—	—	739
b6	0-net B_z	568	$40 \times 370 \times 100$	1	9	1.2	7.2	8.8	—	—	6627
b7	—	563	$60 \times 370 \times 100$	2	—	—	—	—	$\pi/3$	± 0.3	2818
b8	—	316	$54 \times 334 \times 108$	1	3	—	3.7	4.5	$\pi/2$	± 0.2	740
b9	0-net B_ϕ	38	$56 \times 334 \times 108$	2	—	—	—	—	—	—	741
b10	—	40	$36 \times 334 \times 108$	2	—	—	—	—	—	—	750
b11	0-net B_z	80	$34 \times 132 \times 34$	3	—	—	3	3.6	$\pi/3$	± 0.18	1193
b12	—	438	$54 \times 132 \times 64$	4	6	—	—	—	—	± 0.2	1381
n1	net B_z	120	$44 \times 202 \times 54$	3	0.5	—	4	4.8	—	± 0.2	1444
n2	—	360	$34 \times 177 \times 72$	—	—	—	3.7	4.5	—	± 0.18	942
n3	—	120	$44 \times 202 \times 102$	—	—	—	4	4.8	π	± 0.2	628
n4	net B_ϕ	7.6	$34 \times 132 \times 34$	1	—	—	—	—	$\pi/3$	—	1444

Table 1: Parameters associated with the simulations discussed in this paper. The first column gives the simulation label, the second the nature of the initial field, the third the initial value of $\langle\beta\rangle = \frac{\int P d\tau}{\int \mathbf{B}^2/(8\pi) d\tau}$, with the integrals being taken over the Keplerian domain, the fourth the computational grid and the fifth gives the number of wavelengths in the vertical domain of the most unstable MRI mode calculated for the initial field using equation (12). The sixth column gives the number of radial wavelengths in the initial field, and the remaining columns give the boundaries and extents of the radial, azimuthal and vertical computational domains as well as the run time. Models b1, b2, b3, b8, b9, and b10 were all run with heating and cooling exactly in balance while the remainder had an isothermal equation of state with sound speed a fixed function of radius.

can assume they occupy the full 2π when performing azimuthal averages.

We also introduce the surface density

$$\Sigma = \frac{1}{2\pi} \int \rho dz d\phi. \quad (14)$$

Using the above quantities it is possible to describe the angular momentum transport in the disk using functions dependent only on R . In this way a connection to classical viscous disk ‘ α ’ theory can be made (Balbus & Papaloizou 1999).

We monitor the vertically and azimuthally averaged Maxwell and Reynolds stresses, which are respectively defined as follows:

$$T_M(R, t) = 2\pi\Sigma \overline{\left(\frac{B_R(z, R, \phi, t)B_\phi(z, R, \phi, t)}{4\pi\rho} \right)} \quad (15)$$

and

$$T_{Re}(R, t) = 2\pi\Sigma \overline{\delta v_R(z, R, \phi, t)\delta v_\phi(z, R, \phi, t)} \quad (16)$$

The velocity fluctuations δv_R and δv_ϕ are defined through,

$$\delta v_R(z, R, \phi, t) = v_R(z, R, \phi, t) - \overline{v_R}(R, t), \quad (17)$$

$$\delta v_\phi(z, R, \phi, t) = v_\phi(z, R, \phi, t) - \overline{v_\phi}(R, t). \quad (18)$$

With these definitions, the Shakura & Sunyaev (1973) α parameter for the total stress is given by

$$\alpha(R, t) = \frac{T_{Re} - T_M}{2\pi\Sigma \overline{(P/\rho)}}, \quad (19)$$

where the pressure average is taken at the actual time rather than at $t = 0$ as is sometimes found in the literature. With the above definitions the vertically and azimuthally averaged continuity equation (1) may be written

$$\frac{\partial \Sigma}{\partial t} + \frac{1}{R} \frac{\partial (R\Sigma \overline{v_R})}{\partial R} = 0 \quad (20)$$

and the vertically and azimuthally averaged azimuthal component of the equation of motion(2) can be written in the form

$$\frac{\partial (\Sigma \bar{j})}{\partial t} + \frac{1}{R} \left(\frac{\partial (R\Sigma \overline{v_R \bar{j}})}{\partial R} + \frac{\partial (\Sigma R^2 \alpha \overline{P/\rho})}{\partial R} \right) = 0. \quad (21)$$

Here $j = rv_\phi$ is the specific angular momentum. Equations (20) and (21) are identical to what is obtained in viscous ' α ' disk theory (Balbus & Papaloizou 1999). However, as noted by those authors significant differences may occur when the energy balance is considered. From equations (1) and (2) we may derive the rate of energy dissipation, ϵ_ν and doing PdV work per unit volume as

$$\frac{\partial(\rho\epsilon)}{\partial t} + \nabla \cdot \mathbf{F} = -P\nabla \cdot \mathbf{v} - \epsilon_\nu = -Q_T, \quad (22)$$

where, the energy per unit mass and flux are respectively

$$\epsilon = 1/2\mathbf{v}^2 + \Phi + \mathbf{B}^2/(8\pi\rho)$$

and

$$\mathbf{F} = \rho\mathbf{v} \left(1/2\mathbf{v}^2 + \Phi + \frac{\mathbf{B}^2}{4\pi\rho} + \frac{P}{\rho} \right) - \frac{(\mathbf{v} \cdot \mathbf{B})\mathbf{B}}{4\pi}.$$

To reorganize the above into a form more related to ' α ' disk theory we define an energy per unit mass $\epsilon_k(R)$ and specific angular momentum $j_k(R)$. These can be used to define an angular velocity

$$\Omega_k = \frac{\frac{d\epsilon_k(R)}{dR}}{\frac{dj_k(R)}{dR}},$$

and may be chosen to correspond to a free particle in circular Keplerian orbit. The latter assumption is not necessary and any convenient values could be adopted in principle. Note that in the general non Keplerian case $\Omega_k \neq j_k/R^2 = v_k/R$. Performing an azimuthal and vertical average on equation(22) and subtracting (21) after multiplying by Ω_k , we may write the energy balance in an alternative form

$$\frac{\partial(\Sigma\bar{\mathcal{E}})}{\partial t} + \frac{1}{R} \frac{\partial(R\bar{\mathcal{F}})}{\partial R} + \Sigma \left(\bar{v}_R(\bar{v}_\phi - v_k) + \alpha(R)\overline{P/\rho} \right) R \frac{d\Omega_k}{dR} = -\frac{1}{2\pi} \int Q_T dz d\phi. \quad (23)$$

Here

$$\mathcal{E} = \epsilon - \epsilon_k - \Omega_k(\bar{j} - j_k)$$

and

$$\begin{aligned} \mathcal{F} = \Sigma v_R \left(\epsilon - \epsilon_k - \Omega_k(\bar{j} - j_k) + \frac{P}{\rho} + \frac{\mathbf{B}^2}{8\pi\rho} - R\Omega_k\hat{\phi} \cdot (\mathbf{v} - \bar{\mathbf{v}}) \right) \\ - \Sigma(\mathbf{v} - R\Omega_k\hat{\phi}) \cdot \frac{\mathbf{B}B_R}{4\pi\rho} \end{aligned}$$

It can be argued (adopting Keplerian values for ϵ_k, j_k) that in a thin disk that is in a time average near steady state the term proportional to α on the left hand side of (23) is second order in c/v_ϕ , while the others are at least third order (Balbus & Papaloizou 1999). To do

this one needs to extend the azimuthal and vertical average to incorporate an additional time average which is to be carried out over a time long compared to the orbital period but short compared to a supposed much longer evolutionary time scale. The relation of α to energy dissipation that holds in standard ‘ α ’ disk theory is then recovered in the thin disk limit.

However, in some practical cases, including the calculations reported here, which have somewhat large values of $c/v_\phi \sim 0.1$, important deviations may occur. For example the ratio of the contribution of the pressure flux term $\bar{v}_R P$ to the term $\propto \alpha$ in (23) may be estimated as $\bar{v}_R/(\alpha v_\phi)$. In our calculations, at any particular time, this can be of order unity indicating that energy redistribution through pressure wave modes may be important and signaling departures from standard viscous disk theory as far as the energetics is concerned. Thus the adopted ‘ α ’ parameterization may be useful only as far as angular momentum redistribution is concerned. In this context in distinction to standard viscous disk theory, there is no reason why α should be invariably positive. Positive definite dissipation may still occur provided the \mathcal{F} flux terms provide a source (see also Balbus & Papaloizou 1999). In general the magnetic stresses always give a positive contribution to α . However, the contribution of the Reynolds stress can be strongly variable in space, time and sign.

We monitor the average time dependent (radial) Mach number,

$$M_s(R, t) = \frac{\bar{v}_R}{c(R)}. \quad (24)$$

In general \bar{v}_R exceeds the expected mean viscous inflow velocity

$$v_\nu = \alpha c^2 / \bar{v}_\phi \quad (25)$$

appropriate to a Keplerian disk because there are fluctuations in the average radial velocity with near zero mean (compared to their amplitude).

Following Hawley(2000) we use the vertically and azimuthally averaged stresses as a measure of angular momentum transport through $\alpha(R, t)$ defined above. As indicated above one can incorporate a time average with a view to indicating the behavior of a disk evolving on a time scale long compared to the orbital period. The form of the averaged equations given above is unchanged but the mean radial inflow velocity is significantly reduced, becoming comparable to the viscous inflow speed given by equation (25).

In addition, we have considered mean values of α which are obtained from volume averaging over the Keplerian domain. Thus we denote the volume averaged value of α , as a function of t , through

$$\langle \alpha(t) \rangle = \frac{\int_{R_1}^{R_2} \alpha(R, t) R dR}{(1/2)(R_2^2 - R_1^2)}. \quad (26)$$

In practice we find for runs with zero net flux which do not show extreme density contrasts that radial averaging of the total stress over the Keplerian domain (I) gives a value with much reduced temporal fluctuations compared to those occurring at a particular point once the turbulence is established (e.g. the volume average is never negative). Most of the fluctuations seen in our runs appear to be due to the Reynolds stress. Once a time average is performed the contribution of the latter to the total stress is relatively small $\sim 1/3$ in line with local simulations (e.g. HGB96).

Power spectra of the vertically averaged magnetic field components are calculated as the squared Fourier amplitude of an azimuthal mode m as a function of radius as follows

$$|a_{mbi}(R, t)|^2 = \left| \int_{z_l}^{z_u} \int_0^{2\pi} B_i(z, R, \phi, t) e^{-im\phi} d\phi dz \right|^2, \quad (27)$$

where $i = z, R, \phi$.

4. Simulations with zero net flux fields

Provided there is zero field at the radial boundaries, in a global simulation of the type considered here, both the total vertical and the total toroidal flux threading the system are conserved. The latter is guaranteed by the periodic boundary conditions in the vertical direction. As long as there is no flux entry through the radial boundaries simulations can therefore be characterized by the amount of net flux they contain. In particular, if there are no other conserved quantities that can distinguish different simulations, one might expect that (allowing for numerical limitations) all simulations with zero initial net flux should approach the same turbulent state. This has been found to be the case for shearing box simulations (HGB96). However, the shearing box set up is special in that fully periodic boundary conditions in shearing coordinates guarantee no flux entry into the system for all time. In addition, one can search for a time averaged steady state over arbitrary time intervals. The set up of the global simulations considered here only allows for testing that simulations starting with zero net flux approach the same steady state in a more restricted sense. Although we expect magnetic energy to grow through the action of instabilities only in the Keplerian domain, we inevitably find diffusion of field into the inner boundary layer region as well as the outer stable region. When there is significant shear in the boundary

layer region, we find the field can grow through the winding up of the poloidal field to produce a toroidal field with significant magnetic energy. However, this phenomenon may be considerably delayed by starting a simulation with initial field set to be non zero only at large distances from the boundary regions. In this respect we remark that toroidal fields are preferred to vertical fields and the absence of shear in the inner layer delays the build up of strong fields there. In any case there is no guarantee of conservation of magnetic flux in the Keplerian domain once there has been significant field diffusion out of that region. Accordingly, checking whether solutions approach the same turbulent state in the Keplerian domain has been limited to the situation before such diffusion has occurred. If convergence of the solutions occurs, then it should of course hold at a later stage when interaction with the boundary regions occurs. In this context we have found that different prescriptions for the inner boundary layer (i.e. $n_b = 1$ or $n_b = 3$) do not seem to affect the situation in the Keplerian domain even though the behavior in the inner boundary layer region may be significantly different. In this section we investigate the disk response to varying initial fields with zero net flux in order to establish that when these are of small enough radial scale and adequate amplitude essentially the same state results. Other effects such as those of the numerical resolution, disk aspect ratio and size are also explored. We investigate both initially prescribed vertical and toroidal magnetic fields. We find essentially the same final state when the field has a small scale compared to the current radius and a local quasi-steady turbulent state can be achieved on a time scale short compared to the global evolution time of the entire disk. Initial large scale fields with significant magnetic energy may not lead to the same state as small scale fields on a time scale short compared to the evolution time scale of the disk or on one that can be reasonably followed here.

4.1. Disks with initially vertical fields

We first consider the three runs b1, b2, b3 that start from an initial vertical field defined between $R_b = 4/3$ and $R_{b1} = 10/3$. In all of these cases $n_b = 3$ and $n_c = 0.625$ in region II. The runs differ only in the amplitude of the initial vertical field such that the initial $\langle\beta\rangle$ varies by an order of magnitude ranging between ~ 100 and ~ 1000 (see table 1). Many features characteristic for simulations b1, b2, and b3 are also found in others described below. The magnetic energy in the Keplerian domain expressed in units of the volume integrated pressure (or $1/\langle\beta\rangle$) is plotted as a function of time for the three runs in figure 1.

As found with simulations performed in a shearing box (Hawley et al. 1995, Stone et al. 1996, Brandenburg et al. 1995, Ziegler & Rüdiger 2000) and existing global simulations (Hawley 2000, Krolik & Hawley 2000), the simulations with smaller initial $\langle\beta\rangle$ show the

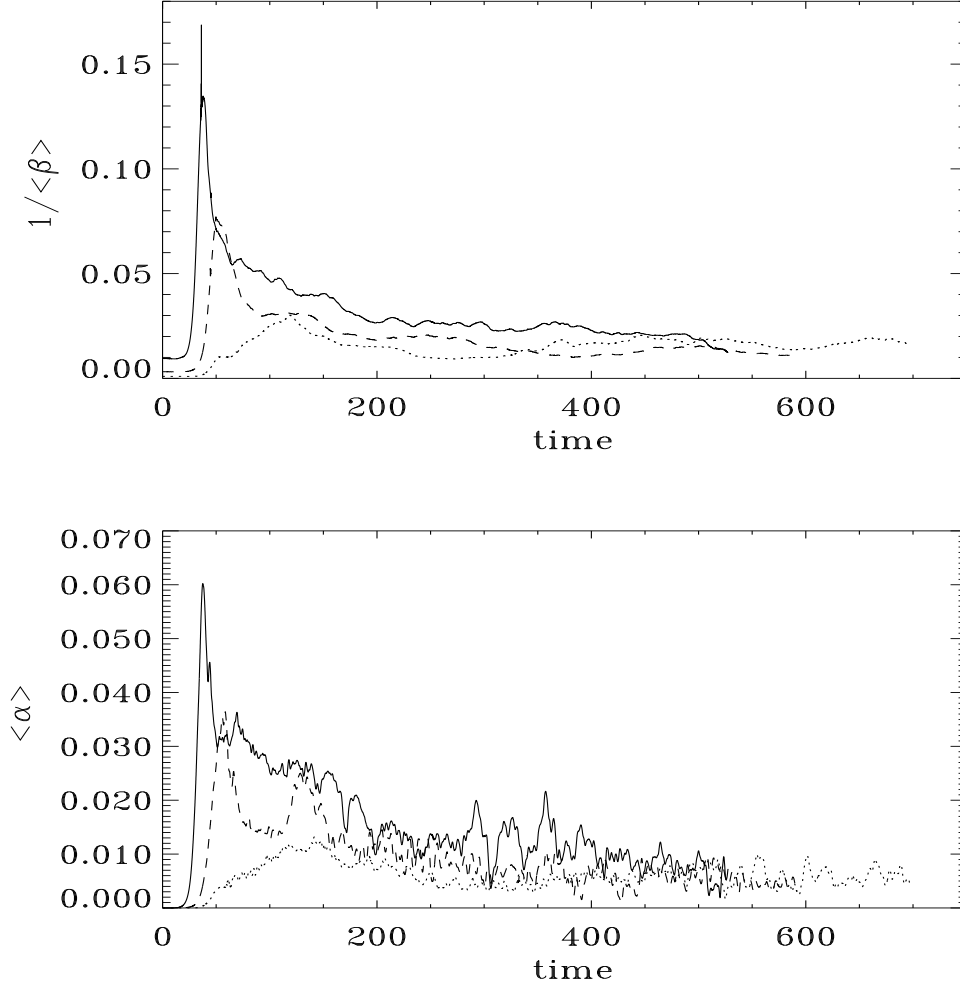


Fig. 1.— Magnetic energy ($1/\langle\beta\rangle$) in the Keplerian domain expressed in units of the volume integrated pressure as a function of time for the three runs b1, b2, b3 (upper panel). Run b1 corresponds to the solid curve and b3 to the dotted curve. In spite of very different initial behavior for $0 < t < 200$ among these cases they all approach a situation where in a time average sense $1/\langle\beta\rangle \sim 0.01$. The value of α volume averaged over the Keplerian domain $\langle\alpha\rangle$ is plotted in the lower panel as a function of time. These, as many other cases, eventually attain $\langle\alpha\rangle \sim 0.005$.

development and growth of channel solutions. This is manifest in the early evolution of b1 through the strong peak in $1/\langle\beta\rangle$ that occurs at $t \sim 30$. Streams of fluid at different vertical levels, alternately moving in opposite radial directions, evolve and persist over a period of several orbits at the corresponding radius. This phase is associated with large values of α peaking at 0.3-0.6 at smaller radii, where the instability grows first due to the smaller rotation period. This behavior is barely noticeable in run b3. We comment that there is not yet a significant penetration of the magnetic field into the boundary regions during the time interval shown. In spite of very different initial behavior for $0 < t < 200$ among these cases they all approach $1/\langle\beta\rangle \sim 0.01$ (in an average sense) as in many other cases we have run (see below). After $t \sim 200$, turbulence is established and maintained throughout the disk. At this stage, it is found that α exhibits strong variations in time and with radial distance, sometimes up to one order of magnitude. The value of α volume averaged over the Keplerian domain $\langle\alpha\rangle$ is plotted as a function of time in the lower panel of figure 1 for the three runs. The volume averaged α shows strong fluctuations on all time scale, which are, however, less than those found at any particular radius. Closer inspection reveals that most of the fluctuation is due to the Reynolds stress which may contribute up to one half of the total. The Maxwell stress is found to be always positive and to vary less strongly.

Simulations b1, b2, b3 attain time averaged values of $\langle\alpha\rangle \sim 0.005$ as in many other cases we have run (see below). This value is similar to what is seen in shearing box simulations starting with weak zero net flux fields (Brandenburg et al. 1995, Hawley et al. 1995). We also comment that we obtain a similar approximate correlation between (R, ϕ) -stress and energy as found in the shearing box simulations of HGB96. This was verified in all simulations with zero net flux and can be expressed, after averaging out short term variations, as $\langle\alpha\rangle \sim 0.5/\langle\beta\rangle$.

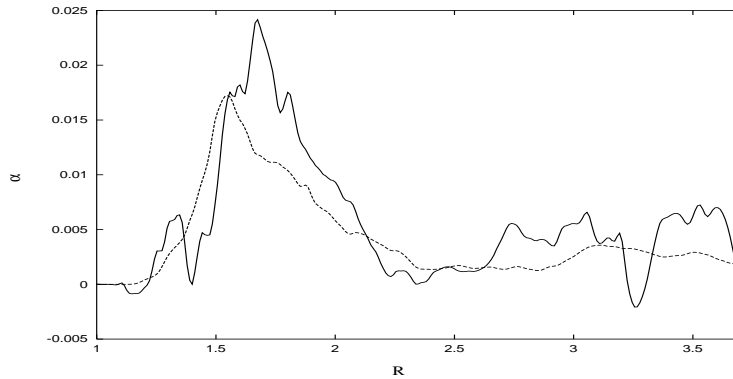


Fig. 2.— In this figure $\alpha(R, t)$ (solid curve) is plotted against dimensionless radius for run b3 at time 643. The dashed curve gives the contribution of the Maxwell stress.

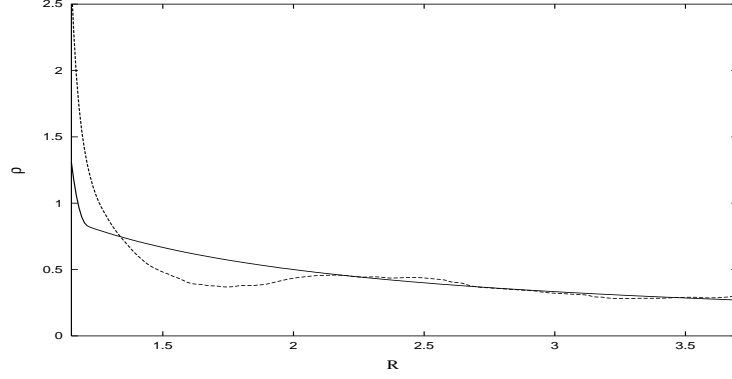


Fig. 3.— Radial dependence of the vertically and azimuthally averaged density (given in arbitrary units) for run b3 at time 643 (dashed line). The initial profile is given by the solid line. Note that at the later time, the density depression apparent between $R = 1.5$ and $R = 2$ together with the density increase at smaller radii is indicative of the mass accretion process.

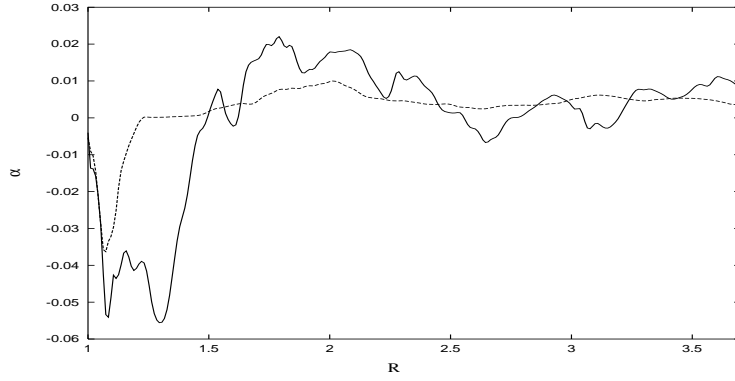


Fig. 4.— Radial dependence of $\alpha(R, t)$ (solid curve) for run b1 at time 540. There is significant field penetration into the boundary layer region as indicated by the negative values there. The Maxwell stress (dashed curve) is also negative in that region.

We plot $\alpha(R, t)$ against radius for run *b3* at time 643 in figure 2. No significant field has yet penetrated into the boundary layer region as can be seen by the small values there. Note that at this time and for this simulation there is a strong peak at smaller radii. However, such a peak may occur in the center of the Keplerian domain at other times and in other simulations (see below). The vertically and azimuthally averaged density corresponding to figure 2 is plotted in figure 3 together with the initial profile. Comparison between the two curves shows evidence of accretion with material moving into the inner region from the outer parts of the disk.

Although it can be delayed by starting with initial data that is non zero far away from the inner boundary layer, the field inevitably diffuses into this region with the degree of penetration increasing with time. This is the case even though the shear indicates stability with respect to the MRI. The pattern of behavior is the same for all runs. For runs *b1*, *b2* and *b3*, which have $n_b = 3$, the strong shear causes the toroidal field to build up and the value of $\alpha(R, t)$ to become negative corresponding to inward angular momentum transport.

As an illustrative example to indicate these points, we plot $\alpha(R, t)$ against radius for run *b1* at time 540 in figure 4. The largest magnitudes of $\alpha \sim -0.05$ occur in this region which tends to expand outwards. Nonetheless, radial motions remain subsonic. Eventually magnetic contact with the inner boundary zones occurs causing a violation of the conditions required for conservation of flux in the computational domain. This effect may be delayed by choosing a more extended inner boundary region.

4.2. Disks with initially toroidal fields and the effect of vertical resolution

We now describe models *b8*, *b9* and *b10*. We set $n_b = 3, n_c = 0.625$ in region II and defined the magnetic field between $R_b = 7/3$ and $R_{b1} = 10/3$ for *b8* and between $R_b = 4/3$ and $R_{b1} = 10/3$ for *b9* and *b10*. These runs were carried out to check that simulations beginning with small scale zero net toroidal fields led to the same state as those starting from vertical fields. For the purpose of comparing with a vertical field run, simulation *b8* started with a poloidal field with the same initial magnetic energy as *b2*, but with higher vertical resolution. Simulation *b10* started with a toroidal field and had the same resolution as *b1*, *b2* and *b3*, while *b9* had higher vertical resolution. Because of the very much weaker instability apparent in the cases with an initial toroidal field, these could be started with significantly larger magnetic energy. No early channel phase occurs. In fact in these cases the magnetic energy decreases due to reconnection of oppositely directed field lines in the initial phases of the MRI.

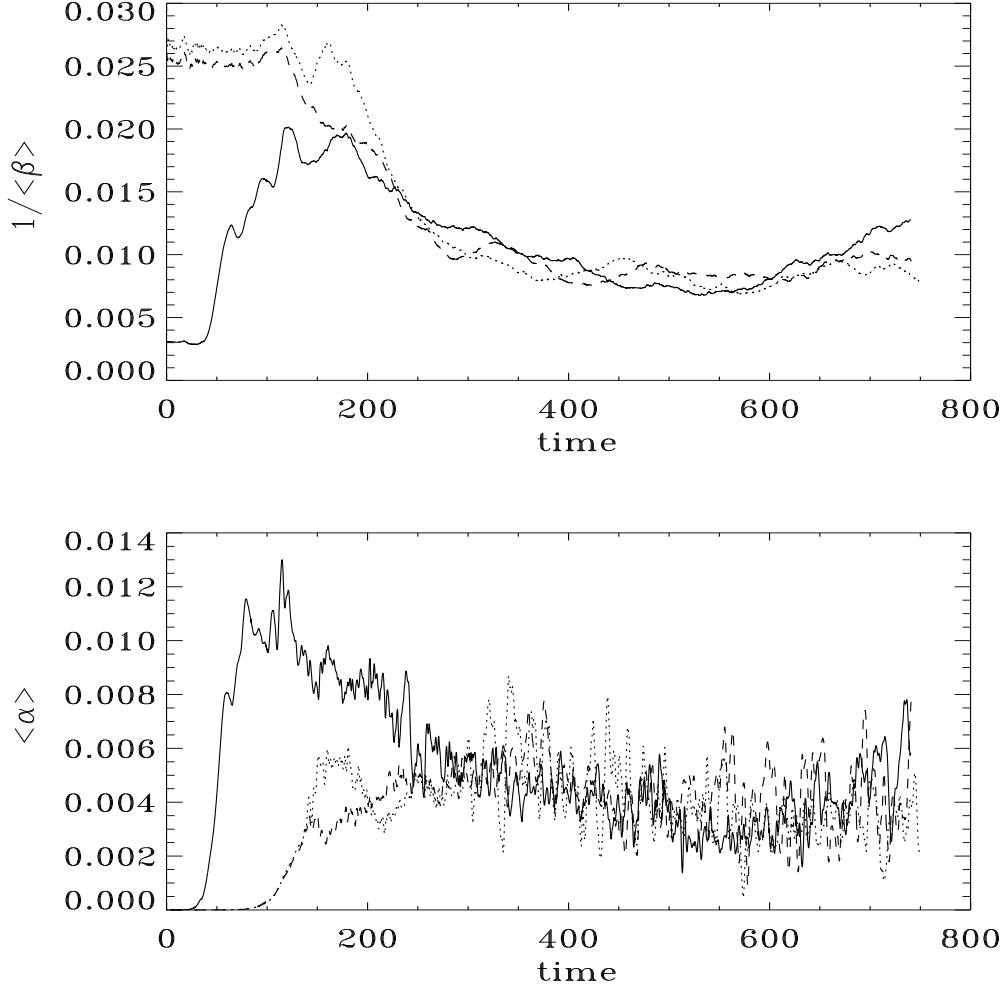


Fig. 5.— Magnetic energy in the Keplerian domain expressed in units of the volume integrated pressure, as a function of time for the three runs b8 (solid curve), b9 and b10 (dotted curve) in the upper panel. The first of these starts with a vertical field while the other two, differing in vertical resolution, start with a toroidal field with significantly larger energy. All these cases eventually approach $1/\langle\beta\rangle \sim 0.01$. In the lower panel the value of α volume averaged over the Keplerian domain $\langle\alpha\rangle$ corresponding to these runs is plotted as a function of time (b8, solid curve, b10, dotted curve).

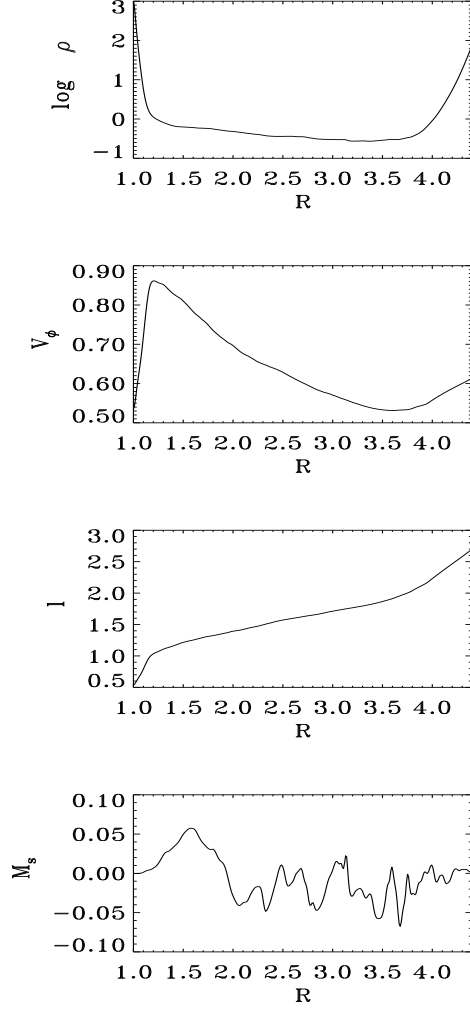


Fig. 6.— From the top panel down, vertically and azimuthally averaged density, azimuthal velocity, specific angular momentum and radial Mach number near the end of simulation b8.

The magnetic energy in the Keplerian domain ($1/\langle\beta\rangle$) expressed in units of the volume integrated pressure is plotted as a function of time for these three runs in the upper panel of figure 5. There is no significant penetration of magnetic field into the boundary regions at this stage. In spite of the different initial conditions and the initially weaker instability in the models starting from a toroidal field, they all eventually attain $1/\langle\beta\rangle \sim 0.01$, as was found for simulations b1, b2 and b3. The increased vertical resolution of simulations b8 and b9 appears to have little influence on the results.

The value of α volume averaged over the Keplerian domain $\langle\alpha\rangle$ is plotted as a function of time for the simulations b8, b9 and b10 in the lower panel of figure 5. These values behave similarly to those found for simulations b1, b2 and b3, and become indistinguishable at later times, with the time averaged value of $\langle\alpha\rangle = 0.004 \pm 0.002$.

For simulation b8 we present in figure 6 the vertically averaged density, azimuthal velocity and radial Mach number profiles near the end of the run. These are similar to the initial profiles.

In order to emphasize the similarity between simulations with initial vertical and toroidal fields with zero net flux in figure 7 we plot the mid plane density contours for simulations b9 and b10 near the end of these runs. Dark regions correspond to low density. Stochastic spiral patterns are visible. In addition, we present the azimuthal power spectra for the vertically averaged magnetic field components calculated according to eq. (27) at $R = 2$ in figure 8. In fact these are characteristic of the turbulent state and are very similar at all radii. There is a flat spectrum for small azimuthal wavenumbers $m < 10$ and a sharp cut-off at $m = 10 - 20$. This behavior is in agreement with the results previously obtained by other authors (e.g. Armitage 1998, Hawley et. al 1995).

4.3. Large disks and long runs

We also ran two simulations, b6, and b7, for which the disk was approximately twice as large as in the previous cases. This has the consequence that the evolutionary time scale for the whole disk is about three times longer. A larger disk enabled insertion of initial magnetic field data further from the inner boundary region with $R_b = 3.5$ and $R_{b1} = 6.5$. In both these models $n_b = 3$ and $n_c = 0.625$ in region II. The resolution in simulation b6 was very similar to the cases discussed above. However, the vertical domain extends over only one half the disk semi thickness in the outer part of the Keplerian domain. In simulation b7, the azimuthal domain was contracted to $\pi/3$ effectively increasing the azimuthal resolution by fifty percent. In addition, the extent of the vertical domain was increased by fifty percent

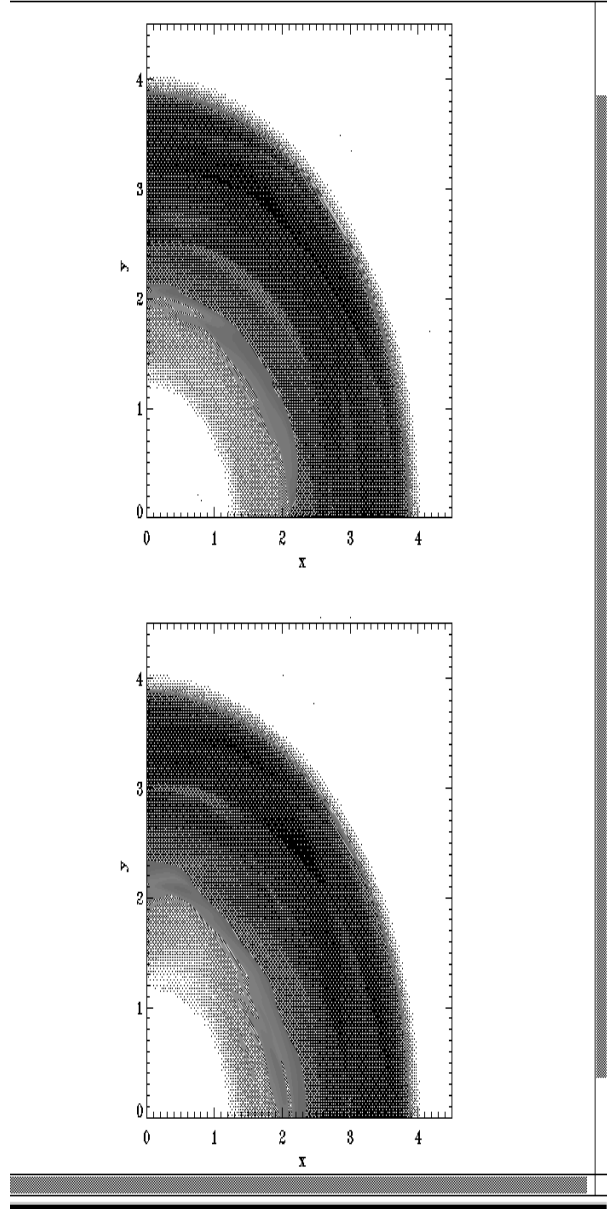


Fig. 7.— Density contours in the mid plane near the end of the runs b8 (upper panel) and b9 (lowe panel). Although these runs start from very different initial conditions, the plots are similar.

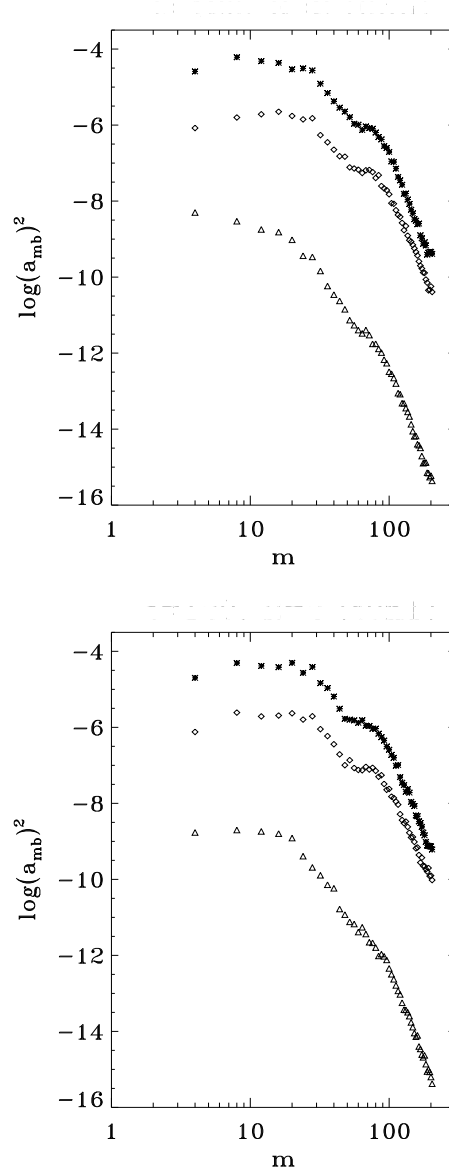


Fig. 8.— Azimuthal power spectra (as defined in the text) of the vertically integrated field components B_ϕ (asterisks), B_R (diamonds) and B_z (triangles) at $R = 2$ for b8 (upper plot) and b9 near the end of their runs. Very similar spectra occur at all radii in the Keplerian domain. Although these runs start from very different initial conditions, the plots are similar.

with respect to b6, while maintaining the same resolution.

The magnetic energy in the Keplerian domain expressed in units of the volume integrated pressure is plotted as a function of time for simulations b6 and b7 in the upper panel of figure 9. These both attain $1/(\langle\beta\rangle) \sim 0.01$ but with some indication of b7 tending to produce larger values than b6. A larger magnetic energy in the saturated turbulent state in b7 might be expected from shearing box simulations (HGB96). These have indicated a dependence on numerical resolution (Brandenburg et al. 1996), as well as larger values for larger boxes. The effect of increasing the size of the vertical domain in b7 is similar to increasing the size of a shearing box. The value of α volume averaged over the Keplerian domain $\langle\alpha\rangle$ is plotted as a function of time for simulations b6 and b7 in the lower panel of figure 9. These attain $\langle\alpha\rangle \sim 0.004 \pm 0.002$ but with b7 tending to give somewhat larger values in the mean. These results are also consistent with the expected correlation between (R, ϕ) -stress and magnetic energy mentioned above in the form $\langle\alpha\rangle \sim 0.5/\langle\beta\rangle$. Simulation b6 indicates survival of the saturated turbulent state for more than fifty orbital periods at the outer boundary of the Keplerian domain. At the end of simulation b7, significant boundary layer penetration occurred producing negative α there. The situation then was very similar to that illustrated in figure 4 for a smaller disk model. Taken together, these simulations indicate some possible dependence of α on numerical resolution and the extent of the vertical domain.

4.4. A thicker disk

Simulations b4 and b5 are characterized by larger semi thickness than the other runs, with $c_0^2 = 0.04GM/R_0$, and a wider uniformly rotating inner boundary layer ($n_b = 1, n_c = 0.625$ in region II and $R_1 = 1.5$). The initial fields were applied between $R_b = 7/3$, and $R_{b1} = 10/3$. These runs were initiated with a zero net poloidal field (b4) and a zero net toroidal field (b5). The initial magnetic energy is about three times larger in b5. These runs have lower absolute radial resolution than those discussed above but the same resolution per scale height. Maintaining the extent of the vertical domain as in the previous runs b1, b2, b3 means that in these two cases only one half of the scale height is contained within the z-domain at the outer edge of the Keplerian domain.

The magnetic energy in the Keplerian domain, $1/(\langle\beta\rangle)$, is plotted as a function of time in the upper panel of figure 10. In spite of the very different initial conditions these simulations both approach a state with $1/(\langle\beta\rangle)$ on average somewhat less than 0.01. The value of α volume averaged over the Keplerian domain $\langle\alpha\rangle$ is plotted as a function of time in the lower panel figure 10. Similar values to those obtained in the other simulations are found.

We also plot $\alpha(R, t)$ as a function of R at time $t = 590$ for simulation b4 in figure 11. This indicates a peak in the center of the Keplerian domain. Even though there is some diffusion of magnetic energy into the boundary layer at about 25 percent of the that in the Keplerian domain. There is little activity in the boundary layer region while there is no contact with the inner boundary zones, because of the low shear. This has been found to be the case in these and other simulations. For the types of computational set up used and the times we have been able to run the simulations, we have found no evidence that the solution in the Keplerian domain is significantly affected by the shear profile adopted in the inner boundary layer. This is found to be the case (not illustrated here) even when runs are continued well beyond the point where magnetic contact with the inner boundary zones occurs.

4.5. Simulations with initial fields with large radial scale of variation

We here describe simulation b11 which had an initial vertical field with zero net flux with a larger scale of radial variation (see table 1) and $n_b = 2$. The field was initially applied between $R_b = 1.32$ and $R_{b1} = 2.76$. This run was carried out with lower resolution than the other simulations but in many ways led to similar results. The large scale motion associated with the channel solutions is completed after $t \sim 240$. After this time, as in other simulations, turbulence is established and maintained throughout the disk. The largest values of $\alpha(R, t) \sim 0.03$ are typically obtained close to the boundary layer and at the outer edge of the Keplerian domain, while in the middle of the active domain, $\alpha(R, t)$ decreases to a mean value of 0.002. The large values of α are connected with vertically and azimuthally averaged density minima there, with a density contrast of up to one order of magnitude with respect to the surroundings. With this type of model, unlike the previously described, convergence of different solutions, if it should occur, is difficult to attain on a reasonable time scale.

As in other simulations, when the magnetic field penetrates the boundary layer region producing an interaction between the boundary layer and the inner regions of the Keplerian disk, the boundary layer moves to a somewhat larger radius (from $R = R_1 = 1.2$ initially to $R \sim 1.36$). The state reached after time 628 is therefore somewhat different from the initial state, with surface density depressions near the boundary layer and the outer stable region. This behavior is typical for initial perturbations with only one to a few wavelengths in the vertical domain for the most unstable MRI mode and an initial field with one to three maxima.

4.6. Oscillations

The vertically and azimuthally averaged radial Mach number remains subsonic throughout the simulations, with the typical radial velocity being ~ 10 times larger than the viscous inflow velocity given by equation (25). It displays oscillatory behavior close to the outer stable boundary region. Such oscillations, which occur in all models, were indicated previously in laminar viscous disk modeling, away from the boundary layer, as a consequence of the viscous overstability found by Kato (1978) (e.g. PS). Here they arise as residuals after averaging turbulent fluctuations vertically and azimuthally and have no obvious connection to the earlier theories because the simple modeling used there does not incorporate the complication that the time and length scales of the oscillations and turbulence are not clearly separable and so do not allow for a description using an anomalous viscosity coefficient. Such a description would only be expected to apply to phenomena on a global length scale averaged over a time scale long compared to that characteristic of the turbulent fluctuations.

In order to further illustrate these oscillations, in figure 12 we have represented the Mach number as a function of time for simulation b12 which had $n_b = 2$ and as in all previously discussed simulations other than b11 was initiated with a small scale field. The superposed curves apply to locations in radius from $R = 2.04$ to $R = 3.04$ in steps of 0.2. The period of the oscillations can be estimated with some noise to be 3.5 expressed in units of the Keplerian period at the inner edge of the computational domain. The Keplerian period corresponding to this range of radii ranges from 2.9 to 5.3. The smaller spread seen in the oscillation periods suggests that they are not entirely purely local epicyclic oscillations but that propagation of information from one location to another occurs in the simulations. A time series of the vertically and azimuthally averaged density as a function of radius performed between two distinct times during the simulation and covering several hundred time units suggests the presence of outward propagating disturbances produced by the interaction between the boundary layer and the Keplerian disk. Some reflection from the boundary of region III may also occur. The phase speed of the waves can be estimated to be a typical sound speed in the Keplerian domain.

5. Simulations with initial vertical fields with net flux

The simulations described above were focussed on conditions starting from small scale fields at small amplitude which lead to a well defined turbulent state in the mean that was, within that framework, initial condition independent. Such a situation would apply to a non magnetic star interacting with a disk threaded by no external flux. However, there may be situations where the disk is threaded with a large scale vertical flux. In that case the disk

is not isolated because conducting material external to the disk is implied as a source. The source could be the material supplied at large distances to the disk itself. Concentration of the flux towards the center of the disk may lead to a large scale poloidal field threading the disk that could be a source of a global outflow as has been considered by many authors (e.g. Blandford & Payne, 1982, Lubow, Papaloizou & Pringle, 1994, Shu et al. 1994, Spruit, Stehle, & Papaloizou, 1995, Konigl & Wardle, 1996). Simulations of disks with net flux may also be relevant to a situation in which the disk becomes dominated by an external magnetic field arising from the central star. The latter point of view was adopted by Miller & Stone (2000) who carried out simulations of a stratified disk in a shearing box. They found magnetically dominated solutions. In their case, vertical gravity was included and outflow boundary conditions were applied in the vertical direction, but Keplerian rotation was enforced by the boundary conditions. In our model this is not the case but there is no vertical stratification. However, the periodic boundary conditions in the vertical direction, neither take into account any constraints arising from the external material in which field lines might be embedded nor correctly match to an external vacuum field. We comment that despite the difference in the models, the outcome is very similar: magnetically dominated solutions.

We here describe simulation n1 with initial mean $\beta = 120$ (see table 1). The magnetic field was applied between $R_b = 1.32$, $R_{b1} = 3.72$ and $n_b = 2$. During the channel phase, the global magnetic energy increases by up to 2 orders of magnitude with respect to the initial value, and drops to a mean value of about one order of magnitude lower than this maximum. This model and other similar ones we ran are characterized by the tendency to produce regions with pronounced density minima or gaps in which the vertically averaged density is smaller by 1-2 orders of magnitude than the surroundings. Conditions in the gaps were strongly variable, with inhomogeneous variations in z and ϕ of sometimes more than one order of magnitude. This inhomogeneity is evident in figure 13 where we show polar contours of the surface density (upper panel) along with a slice of the density in the R-z-plane ($\phi=0$) at time 1224. The gaps, one located next to the boundary layer, and a second near to the outer stable region, are visible as lumpy structures in azimuth, and radially elongated low-density filaments alternating with large density regions are visible in the R-z plane. This picture remains qualitatively unchanged throughout the simulation (1444 time units).

The formation and survival of the gaps appears to be a characteristic of initial vertical fields with large net flux, which in turn have strong initial channel solutions. After an associated reconnection, a net vertical magnetic flux is trapped in low density regions with a radial extent larger than one local scale height. A large scale vertical field persists in association with the gaps. In the bottom panel of figure 13 we show the magnetic field vectors in the R-z plane ($\phi = 0$) at time 1224. Superimposed is a binary map of the critical wavelength

λ_c (white represents stable regions). Note that the inner gap extends roughly from 1.2 to 2, while the outer gap is located from 3.2 to 4. When the critical wavelength exceeds the disk height, the angular momentum transport from the faster to the slower rotating regions is mediated by the torque exerted by the toroidal field that is built up from the poloidal field. The toroidal field is wound up until torque balance occurs maintaining the gap. This mechanism operates analagous to magnetospheric cavity formation (e.g. Ghosh & Lamb 1978). In that case, a poloidal field is wound up between the disk and the central star rotating at a different rate until a steady torque is transmitted between the two via a force-free field. At the edges of the gap, the axisymmetric MRI can always operate, as the condition for instability is fulfilled. Indeed, figure 13 shows that the field stretches out radially across the gaps until it reconnects. Filaments or blobs of magnetic flux are expelled from both sides of the gaps, and a concentration of vertical flux is left there. In this manner, the large-scale field is maintained in the gap by the MRI.

We find large values of α correlated with the low density within the gaps. The upper panel of figure 14 shows the radial dependence of α at time 1143, while the lower panel represents the time evolution of the volume averaged α . α periodically becomes larger than unity in the regions corresponding to the gaps. In some models, values of α as large as 3 can be attained (this finding being in agreement with Hawley (2001)). The Maxwell stress dominates over the Reynolds stress there, while outside the gaps, the Reynolds stress becomes important. Outside the gaps, α may decrease to a mean of 0.005, similar to the zero net field models.

When gaps are formed next to the boundary layer, the large-scale poloidal magnetic field trapped in that region contributes to link the boundary layer to the outer disk. A periodic broadening and narrowing of the boundary layer becomes evident in this case. We attribute this oscillation to the interaction between the disk and the boundary layer via the field connecting these regions. A time sequence of azimuthally and vertically averaged density profiles (represented in figure 15) shows that waves, most likely excited by this oscillation of the boundary layer propagate through the high density region exterior to the gap.

We performed a number of simulations with varying resolution (e.g. run n2) and computational domain (e.g. n3). All these runs show the formation of at least one prominent gap (located next to the boundary layer) and the presence of one or two smaller gaps which have the tendency to deepen with time and sometimes merge. Their position may vary slightly with resolution and extent of the radial or azimuthal domain. These findings are in agreement with Hawley (2001).

5.1. A simulation with a toroidal field with net flux

Simulation n4 was performed with an initial toroidal field with net flux and with one maximum in R . The magnetic field was applied between $R_b = 1.32$ and $R_{b1} = 2.76$ and $n_b = 2$. As in the cases with zero net flux, the instability is weak when compared to models with an initial vertical field. The magnetic energy first shows growth after time 125.6 peaking after 289 then having grown by a factor of two. A quasi-steady turbulent state was reached after about 377 time units, with the global magnetic energy being 0.8 of the initial value at the end of the simulation (time=1444). The radial variations of the vertically and azimuthally averaged stress parameter α are relatively small, not exceeding a factor of 3. The lower panel of figure 16 shows the time variation of α at $R=2$, and indicates a mean value of 0.04. In the upper panel, we represent the radial dependence of α close to the end of the simulation (t=1388). The magnetic stress is always dominant, and the Reynolds stress can sometimes become negative as previously discussed and the boundary layer moves slightly inwards in the course of the simulation.

6. Discussion

In this paper we have studied the time dependent evolution of a near Keplerian accretion disk which rotates between two bounding regions with initial rotation profiles that are stable to the MRI. The inner region models the boundary layer between the disk and a central star. Because we self-consistently incorporate MRI-induced turbulence as the source of viscosity, the necessity of an ad-hoc viscosity prescription of the type used in earlier studies is removed.

For this first study we assumed the disk to be unstratified with aspect ratio $H/R \simeq 0.1 - 0.2$ by adopting a cylindrically symmetric potential assumed to be exclusively generated by the central object. For most of the cases considered, the dynamical evolution of the disk following from the imposition of different magnetic field configurations was followed over a time span between one hundred and two hundred rotation periods at the inner edge of the computational domain. However, simulations of radially more extended disks were followed up to one thousand orbital periods at the inner edge of the computational domain. For initial conditions both toroidal and poloidal magnetic fields with zero as well as net flux were applied in varying domains contained within the near Keplerian disk.

Simulations starting from toroidal and poloidal fields with zero net flux and a small scale of radial variation evolved to a state characterized by a smooth angular velocity and density profile similar to the initial one. This was independent of the type, and within numerically determined limits, the amplitude of the initial field. This result also holds in shearing

box simulations (HGB96). But one must bear in mind that in numerical computations, the range of initial plasma betas to which one has reasonable access is restricted by the resolution. Typical values of $\langle\alpha\rangle$ representing a volume average over the Keplerian domain are 0.004 ± 0.002 . Moreover, runs with a radially extended disk showed that the saturated turbulent state is maintained over more than fifty orbital periods at the outer boundary of the Keplerian domain.

While the shearing box approach guarantees flux conservation for all time in a Keplerian domain, in global simulations this is not necessarily the case. This is because in large scale simulations the inevitable diffusion of the magnetic field out of the Keplerian domain and into the boundary domains can lead to the violation of flux conservation in the Keplerian domain. This happens even though the boundary domains are stable to the MRI. However, we found that different prescriptions of the inner boundary layer region do not affect the final state in the Keplerian domain even though the behavior of the boundary layer itself may vary significantly. Once significant field has leaked into the boundary layer, toroidal field is built up due to the shear and causes α to attain negative values corresponding to inward angular momentum transport and mass accretion. In such cases, the boundary layer expands outwards but radial motions remain subsonic.

We also find a similar approximate correlation between the Keplerian domain volume averaged $(R\phi)$ -component of the stress and magnetic energy as found in local simulations: For simulations with zero net flux we find, after averaging out short term variations, $\langle\alpha\rangle \sim 0.5/\langle\beta\rangle$.

Models with an initial vertical field with zero-net flux and large scale of radial variation exhibit local minima in the density associated with maxima of the angular velocity. These density pockets can reach a contrast of one order of magnitude with respect to the surroundings. The turbulent state can nonetheless be characterized by an average α similar to the cases with small scale of radial variation. It may require a very long time scale for such states to relax to those found in the initially small scale field cases.

All models display large variations of α in time and radius including oscillations on a rotational time scale. Variations of one order of magnitude are typical.

Models starting with fields that have non zero net flux lead to a higher level of turbulence. Thus, model n4 that started with a toroidal field attains an average alpha of 0.04. Those starting with vertical fields with net flux such as n1 may display several gaps in density, with the radially innermost gap typically located next to the boundary layer. The density contrast in the most prominent gaps can reach up to 2 orders of magnitude (in an azimuthal and vertical average) with respect to their surroundings. In the gap-regions, α alternates

between values < 1 and > 1 , sometimes exceeding 3 and dropping to an average of 0.005 (comparable with the zero net flux simulations) in non gap regions. Values of α exceeding 1 indicate angular momentum transport by magnetic torques originating from fields that connect across the gap region.

Recognizing that there are issues to be resolved regarding the correct boundary conditions required to represent the effects of external conducting material, these solutions might be relevant when the disk becomes dominated by an external magnetic field. Such magnetic fields may affect a variety of processes that take place in accretion disks, from dust coagulation to the interaction of planets with the disks in which they have been formed.

Clearly there is much room for future improvements and developments. Convergence needs to be checked at much higher resolution than currently attainable. Studies of more extended inner MRI-stable boundary layers should be carried out, and vertical stratification should be included. In this connection the simple periodic boundary conditions used in the vertical direction leave the vertical flux relatively unconstrained and unconnected to any conductors external to the disk. Proper matching of boundary conditions to external fields is also an issue that may affect the behavior of the low density gap regions studied here and a subject for future study.

6.1. Acknowledgements

We would like to thank Richard Nelson for encouragement and support regarding computational matters and him together with Caroline Terquem and Greg Laughlin for valuable discussions. We acknowledge support from the UK Astrophysical Fluids Facility and the NASA Advanced Supercomputing Facility’s Information Power Grid Project’s Pool at NASA ames Research Center. AS thanks the Astronomy Unit at QMW for hospitality, the European Commission for support under contract number ERBFMRX-CT98-0195 (TMR network “Accretion onto black holes, compact stars and protostars”) and the NRC for a research fellowship.

REFERENCES

- Armitage, P. J., 1998, ApJ, 501, L189
- Balbus, S. A., Hawley, J. F., 1991, ApJ, 376, 214
- Balbus, S. A., Papaloizou, J. C. B., 1999, ApJ, 521, 650

- Blandford, R. D., Payne, D. G., 1982, MNRAS, 199, 883
- Blumenthal, G. R., Yang, L. T., Lin, D. N. C., 1984, ApJ, 287, 774
- Brandenburg, A., Nordlund, Å., Stein, R. F., Torkelsson, U., 1995, ApJ, 446, 741
- Brandenburg, A., Nordlund, Å., Stein, R. F., Torkelsson, U., 1996, ApJ, 458, L45
- Bryden, G., Chen, X., Lin, D. N. C., Nelson, R. P., Papaloizou, J. C. B., 1999, ApJ, 514, 344
- Fleming, T. P., Stone, J. M., Hawley, J. F., 2000, ApJ 530, 464
- Ghosh, P., Lamb, F. K., 1978, ApJ, 223, L83
- Hawley, J. F., Gammie, C. F., Balbus, S. A., 1995, ApJ, 440, 742
- Hawley, J. F., Stone, J. M., 1995, Computer Physics Communications, 89, 127
- Hawley, J. F., Gammie, C. F., Balbus, S. A., 1996, ApJ, 464, 690 (HGB96)
- Hawley, J. F., 2000, ApJ, 528, 462
- Hawley, J. F., 2001, ApJ, 554, 534
- Hawley, J. F., Krolik, J. H., 2001, ApJ, 548, 348
- Kato, S., 1978, MNRAS, 185, 629
- Kley, W., 1989, A&A, 208, 98
- Kley, W., Papaloizou, J. C. B., 1997, MNRAS, 285, 239
- Kley, W., D’Angelo, G., Henning, 2001, Th., ApJ, 547, 457
- Konigl, A., Wardle, M., 1996, MNRAS, 279, L61
- Lightman, A. P., Eardley, D. M., 1974, ApJ, 187, L1
- Lubow, S. H., Papaloizou, J. C. B., Pringle, J. E., 1994, MNRAS, 267, 235
- Lynden-Bell, D., Pringle, J. E., 1974, MNRAS, 168, 603
- Miller, K. A., Stone, J. M., 2000, ApJ, 534, 398
- Narayan R., 1992, ApJ, 394, 261

- Nelson, R. P., Papaloizou, J. C. B., Masset, F., Kley, W., 2000, MNRAS, 318, 18
- Papaloizou, J. C. B., Stanley, G. Q. G., 1986, MNRAS, 220, 593 (PS)
- Popham R., Narayan R., 1992, ApJ, 394, 255
- Pringle, J. E., 1977, MNRAS, 178, 195
- Sano, T., Inutsuka, S.-I., Miyama, S. M., 1998, ApJ, 506, L57
- Shakura, N. I., Sunyaev, R. A., 1973, A&A, 24, 337
- Shu, F., Najita, J., Ostriker, E., Lizano, S., 1994, ApJ, 429, 781
- Spruit, H. C., Stehle, R., Papaloizou, J. C. B., 1995, MNRAS, 275, 1223
- Stone, J. M., Hawley, J. F., Gammie, C. F., Balbus, S. A., 1996, ApJ, 463, 656
- Ziegler, U., Rüdiger, G., 2000, A&A, 356, 1141

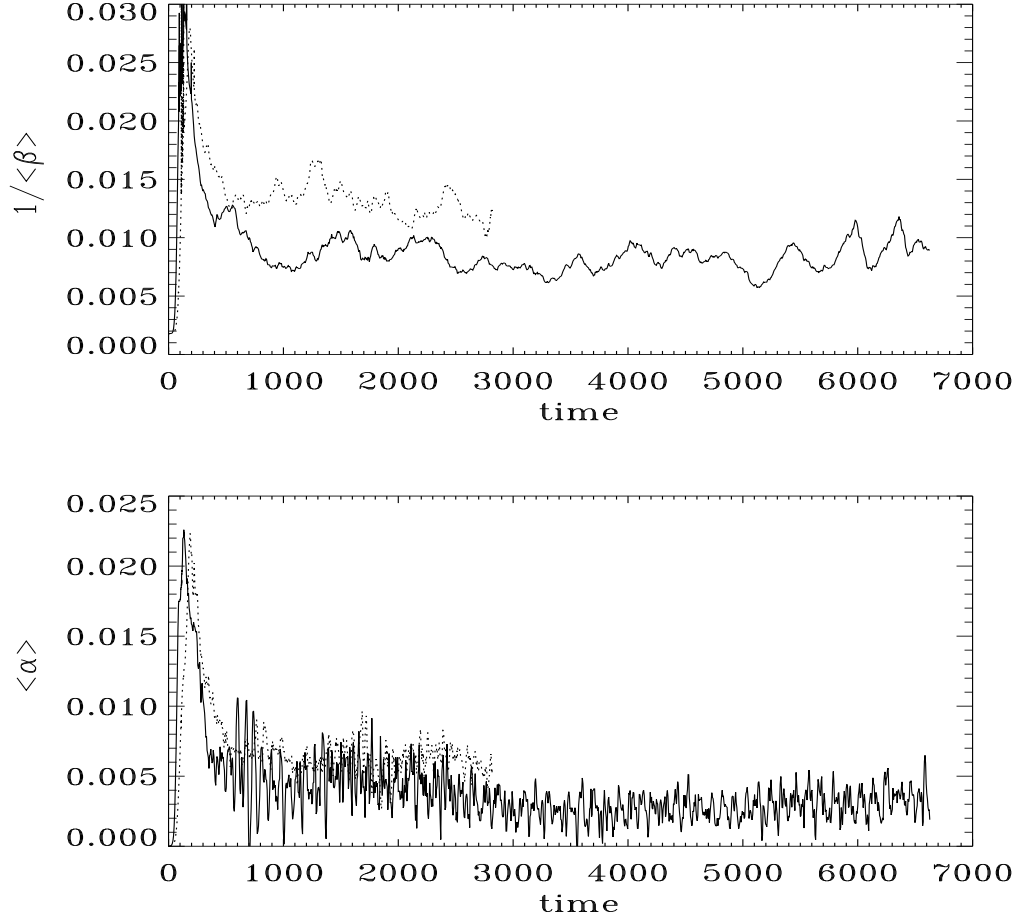


Fig. 9.— Magnetic energy in the Keplerian domain (in units of the volume integrated pressure) plotted as a function of time (upper panel) for the large disk runs b6 (solid curve) and b7. In the lower panel we represented $\langle\alpha\rangle$ as a function of time for these runs.

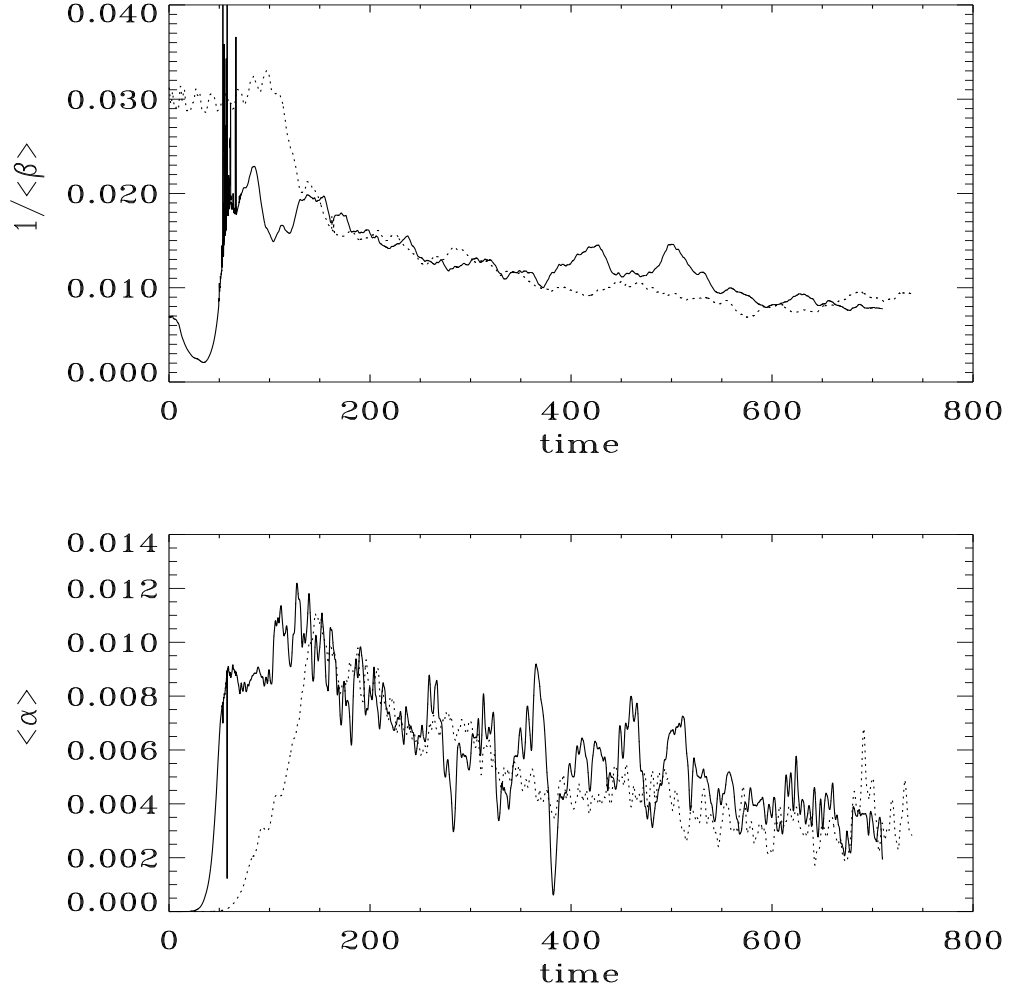


Fig. 10.— Magnetic energy in the Keplerian domain expressed in units of the volume integrated pressure as a function of time (upper panel) for the thick disk runs b4 (solid curve) and b5. The corresponding value of α volume averaged over the Keplerian domain $\langle\alpha\rangle$ as a function of time is represented in the lower panel.

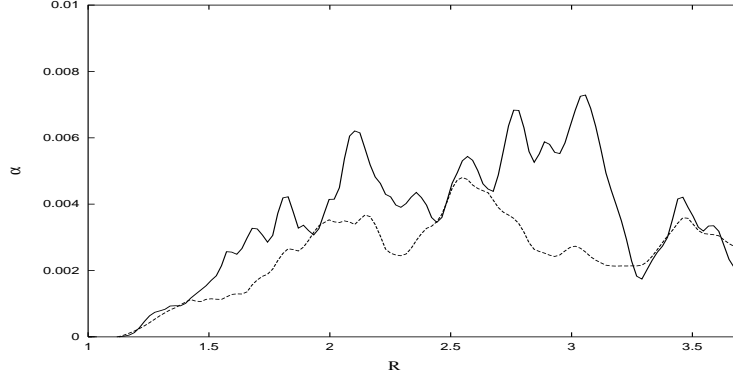


Fig. 11.— Radial dependence of $\alpha(R, t)$ (solid curve) for run *b4* at time 590. The dashed curve gives the contribution of the Maxwell stress.

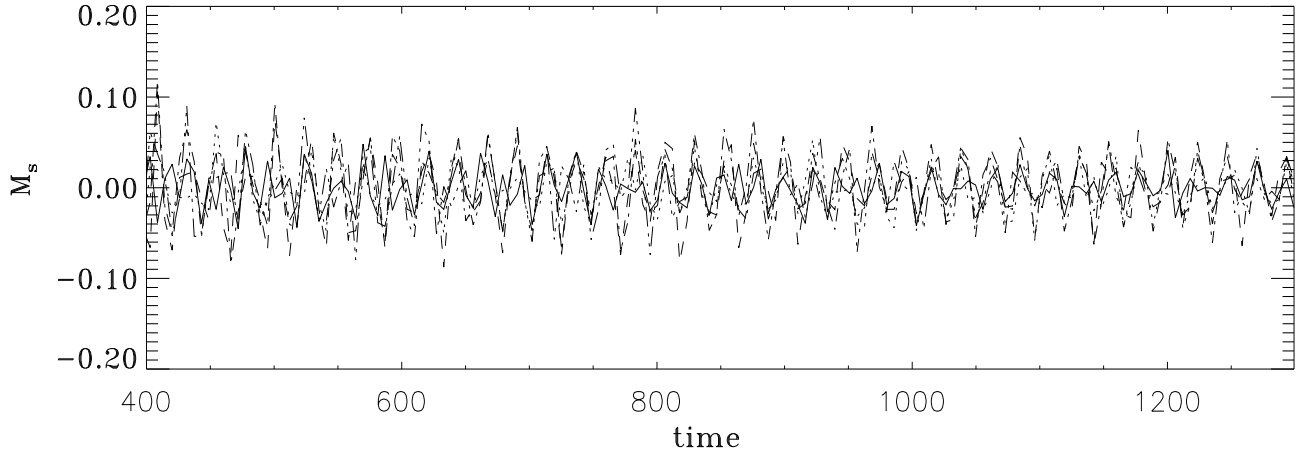


Fig. 12.— Time evolution of the azimuthally and vertically averaged Mach number at different radii, from $R=2.04$ to 3.04 in steps of 0.2 for run *b12*.

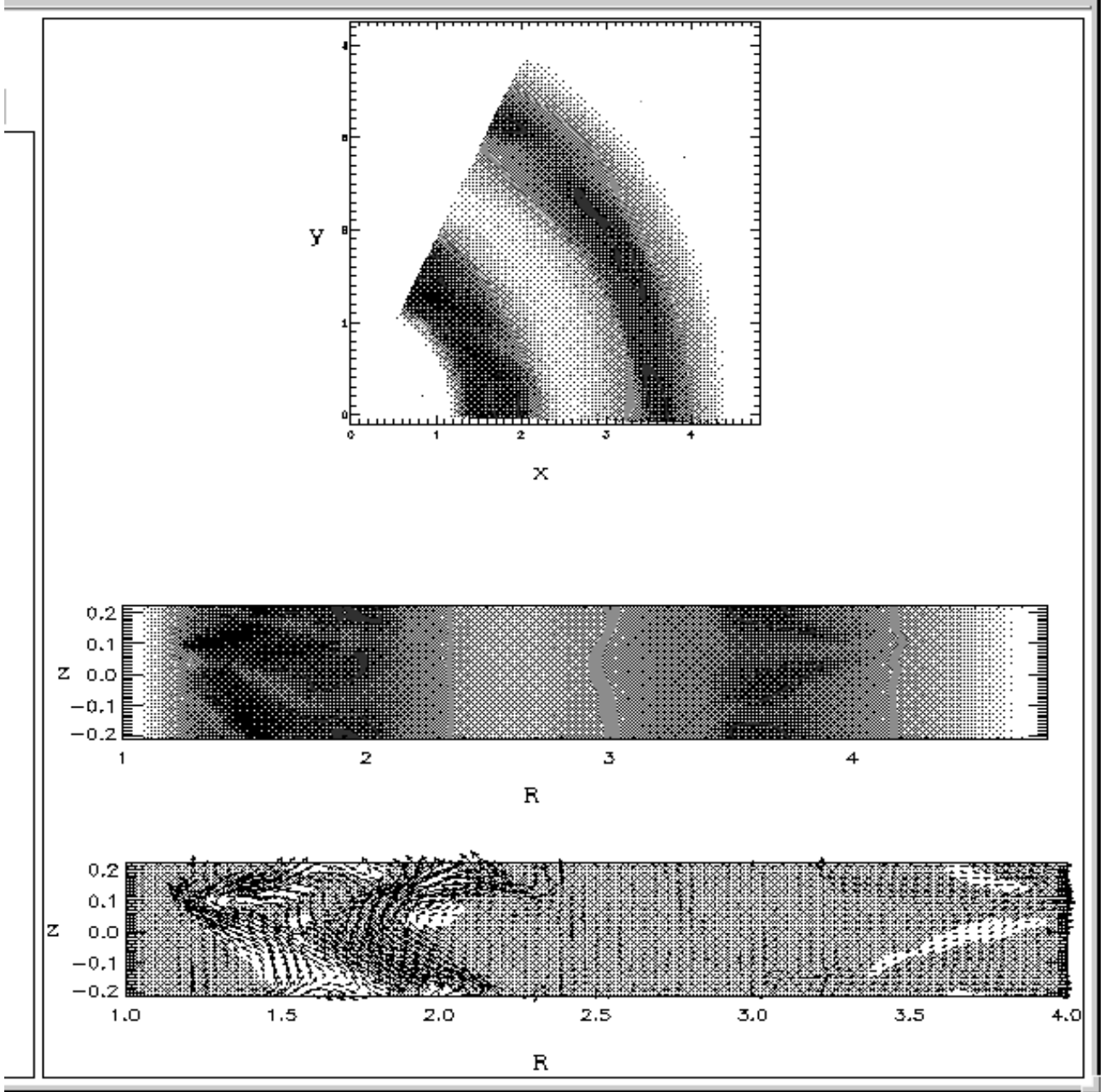


Fig. 13.— Polar contours of the surface density (upper panel) along with the density in the R - z -plane at $\phi = 0$ and time 1224 for model n1. The bottom panel shows the poloidal magnetic field vectors with the superimposed binary map of the critical wavelength of the MRI. White regions correspond to λ_c exceeding the disk height.

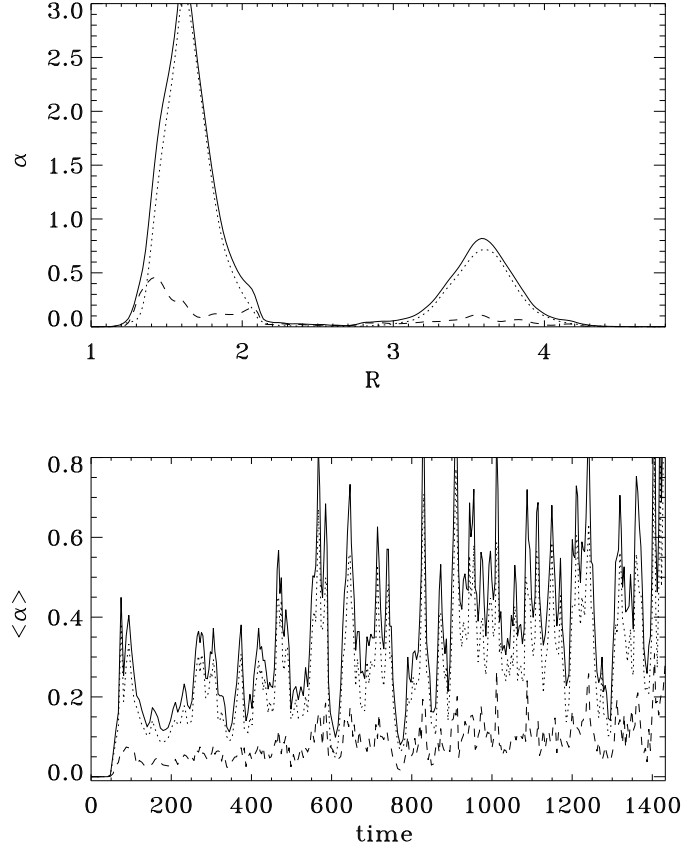


Fig. 14.— Radial dependence of α for time 1143 (upper panel) and time evolution of the volume averaged α (lower panel) for run n1. The dotted curve represents the magnetic stress contribution and the dashed curve the Reynolds stress contribution.

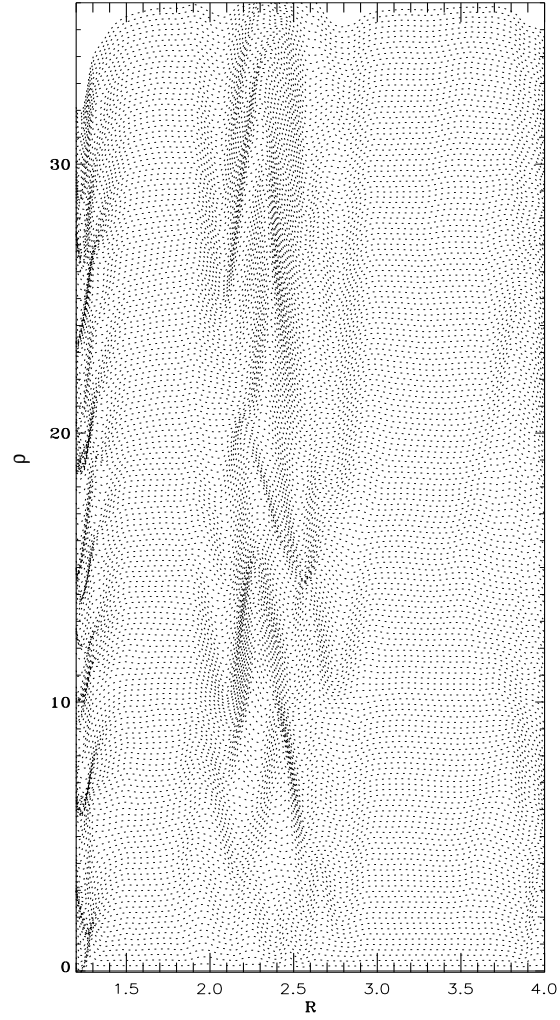


Fig. 15.— Time sequence of the averaged density for model n1 between time 565 and 609.

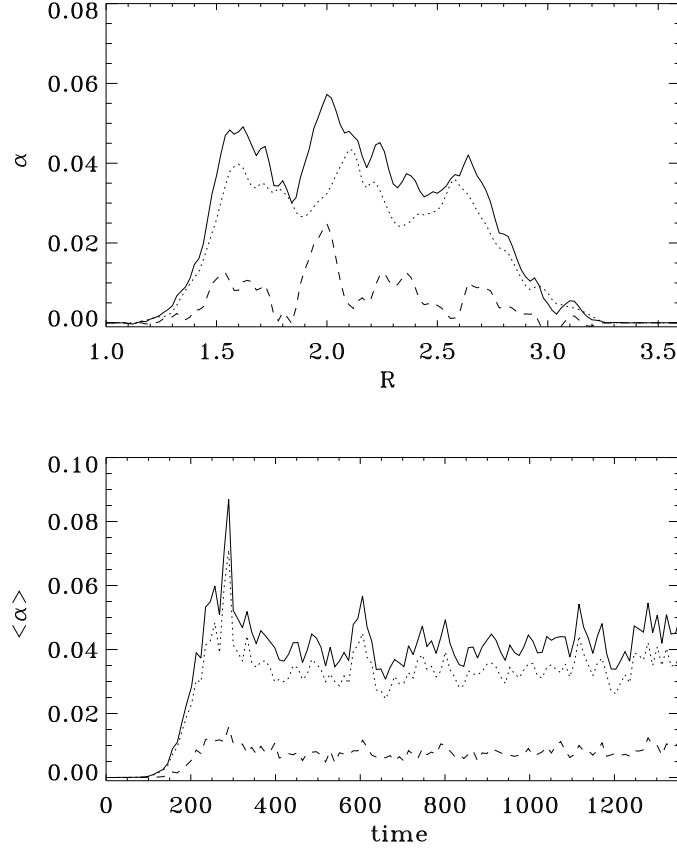


Fig. 16.— Radial dependence of α for $t=1388$ (upper panel) and time evolution of the volume averaged α (lower panel) for run n4. The dotted curve represents the magnetic stress contribution and the dashed curve the Reynolds stress contribution.